

This item was submitted to [Loughborough's Research Repository](#) by the author.  
Items in Figshare are protected by copyright, with all rights reserved, unless otherwise indicated.

## **Laser sintering and patterning of gallium-doped zinc oxide/indium-tin oxide nanoparticle films with tailorable electrical and optical properties**

PLEASE CITE THE PUBLISHED VERSION

<https://doi.org/10.1016/j.matdes.2020.108865>

PUBLISHER

Elsevier BV

VERSION

VoR (Version of Record)

PUBLISHER STATEMENT

This is an Open Access Article. It is published by Elsevier under the Creative Commons Attribution 4.0 Unported Licence (CC BY). Full details of this licence are available at:  
<http://creativecommons.org/licenses/by/4.0/>

LICENCE

CC BY 4.0

REPOSITORY RECORD

Wang, Jing, Fabiana Lisco, David Hutt, Lewis Jones, Jake Bowers, Patrick Isherwood, Zhaoxia Zhou, and Paul Conway. 2020. "Laser Sintering and Patterning of Gallium-doped Zinc Oxide/indium-tin Oxide Nanoparticle Films with Tailorable Electrical and Optical Properties". Loughborough University.  
<https://hdl.handle.net/2134/12579866.v1>.



# Laser sintering and patterning of gallium-doped zinc oxide/indium-tin oxide nanoparticle films with tailorable electrical and optical properties

Jing Wang<sup>a,\*</sup>, Fabiana Lisco<sup>b,1</sup>, David A. Hutt<sup>a,\*</sup>, Lewis C.R. Jones<sup>a</sup>, Jake W. Bowers<sup>b</sup>, Patrick J.M. Isherwood<sup>b</sup>, Zhaoxia Zhou<sup>c</sup>, Paul P. Conway<sup>a</sup>

<sup>a</sup> Wolfson School of Mechanical, Electrical and Manufacturing Engineering, Loughborough University, Loughborough LE11 3TU, UK

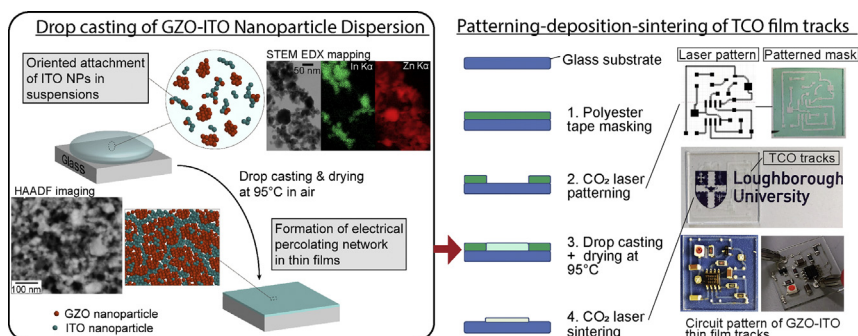
<sup>b</sup> Centre for Renewable Energy Systems Technology (CREST), Wolfson School of Mechanical, Electrical and Manufacturing Engineering, Loughborough University, Loughborough LE11 3TU, UK

<sup>c</sup> Loughborough Materials Characterisation Centre, Department of Materials, Loughborough University, Loughborough LE11 3TU, UK

## HIGHLIGHTS

- Drop cast films of Gallium-doped Zinc Oxide(GZO)/Indium Tin Oxide(ITO) nanoparticles
- Rapid CO<sub>2</sub> laser sintering of GZO/ITO nanoparticle films and circuit patterns
- Additions of ITO stabilise aqueous GZO dispersions and improve film quality.
- GZO/ITO ratio controls resistivity, near-infrared transmittance and optical bandgap.
- Low levels of ITO in the film significantly reduce resistivity compared to pure GZO.

## GRAPHICAL ABSTRACT



## ARTICLE INFO

### Article history:

Received 3 February 2020  
Received in revised form 4 June 2020  
Accepted 5 June 2020  
Available online 6 June 2020

### Keywords:

Transparent conducting oxide  
Indium tin oxide  
Gallium doped zinc oxide  
Nanoparticles  
Laser processing  
Patterning

## ABSTRACT

Gallium-doped zinc oxide (GZO) and tin-doped indium oxide (ITO) nanoparticles (NPs) were combined to create bi-component suspensions for the drop-casting and CO<sub>2</sub>-laser sintering of transparent conducting oxide (TCO) thin films with significantly reduced ITO content. An aqueous dispersion of ITO NPs enabled the suspension of GZO NPs without surfactants. Transmission electron microscopy indicated the formation of high aspect-ratio segments of ITO NPs from the suspension through oriented attachment, that persisted in the deposited and sintered thin films to establish an efficient electrical percolating network within the less conductive GZO NP matrix. Rapid CO<sub>2</sub>-laser sintering under argon gas of approximately 800 nm thick NP films yielded resistivities of  $7.34 \times 10^{-3} \Omega \cdot \text{cm}$  and  $116 \Omega \cdot \text{cm}$  for pure ITO and pure GZO respectively. However, a bi-component film with only 19.6 at.% indium (relative to zinc) achieved a resistivity of  $3.21 \times 10^{-1} \Omega \cdot \text{cm}$ . By changing the ITO content, the near-infrared transmittance could be adjusted between 13% and 82% and the optical bandgap energy between 3.93 and 3.33 eV, enabling fine-tuning of the properties. Finally, a fast and material/energy efficient processing route was demonstrated for the fabrication of a GZO-ITO circuit pattern using CO<sub>2</sub>-laser patterning of a mask and CO<sub>2</sub>-laser sintering of the NP films.

© 2020 The Authors. Published by Elsevier Ltd. This is an open access article under the CC BY license (<http://creativecommons.org/licenses/by/4.0/>).

## 1. Introduction

Transparent conducting oxides (TCOs) are degenerately doped metal oxides displaying a unique combination of electrical conductivity and optical transparency and are of great importance to a wide range of

\* Corresponding authors.

E-mail addresses: [J.Wang6@lboro.ac.uk](mailto:J.Wang6@lboro.ac.uk) (J. Wang), [D.A.Hutt@lboro.ac.uk](mailto:D.A.Hutt@lboro.ac.uk) (D.A. Hutt).

<sup>1</sup> Present address: PV-LAB EPFL, Rue de la Maladière 71b, CH-2000 Neuchâtel, Switzerland.

applications including touch screens, flat panel displays, light emitting devices, thin film photovoltaics, plasmonic devices, electrochromic devices and sensors [1–5]. For most applications, indium-oxide based TCOs such as tin-doped indium oxide (ITO) have thus far remained largely unrivalled owing to their inherently high carrier concentrations [6], excellent optical properties [7] and relatively good chemical stability [8]. The unsustainable supply and volatile cost of indium (In) have nonetheless necessitated the search for strategies towards reducing indium consumption. More sustainable alternatives such as gallium-doped zinc oxide (GZO) [9] and aluminium-doped zinc oxide (AZO) [10] have shown great promise. They are typically reported to exhibit higher transparency in the infrared (IR) wavelength region [11], albeit with lower electrical conductivity and inferior stability in air and moisture [12] when benchmarked against ITO [13].

The industrial pursuit of high efficiency and multifunctional devices entails a broader design scope over the material and structure of TCOs to enable tailored functionalities while ensuring durability. For example, long-term stability of high electrical conductivity is crucial for applications such as sensors where transparent electrodes may be exposed to air or other environments in service. In addition, optical properties require tailoring for specific applications: for instance increased near-infrared absorption is desirable for plasmonic devices, such as switches at telecommunication wavelengths and waveguide modulators [14,15] whereas high transmittance across the visible and near-infrared spectrum is required for enhanced efficiency in thin film solar cells [16,17]. For applications where ITO cannot thus far be effectively replaced, ensuring high processing efficiency and low material loss is key to the sustainable manufacture of ITO-based products. This can become particularly effective in concert with ever maturing end-of-life recycling technologies where, for example, in 2016 approximately 1200 t/yr of indium was reclaimed from used products compared with an annual ITO global consumption rate of approximately 1500 t/yr [18].

In addition to sputtering [19], chemical vapour deposition [20], sol-gel [21], spray pyrolysis [22] and chemical bath deposition [23] of TCO thin films, the deposition of colloidal nanoparticles (NPs) has attracted interest owing to fast film thickness build-up and low material loss. When working with nanoparticulate TCOs, in order to achieve the desired material properties, it is necessary to sinter together the particles to ensure low electrical resistance contacts between them [24,25]. This is often achieved through a thermal process undertaken in an inert or reducing atmosphere, such as conventional thermal treatments or microwave irradiation [6,26,27]. However, it has been shown that similar levels of conductivity can be achieved in a fraction of the time using a laser to anneal thin films of nanoparticles. Königer et al. [28] used a CO<sub>2</sub> laser to sinter spin-coated ITO NP thin films in air, while Park and Kim [29] employed an excimer laser to anneal spin-coated ITO NP coatings in a nitrogen ambient. They achieved electrical resistivities similar to those of furnace annealed materials, but in only tens of seconds. In addition, they demonstrated the processing of ITO films on temperature-sensitive substrates such as polyethylene terephthalate [28,29] by utilising the highly controlled delivery of the laser energy into the nanoparticle film, with only limited heat transfer to the substrate.

Single component TCO materials do not always meet the challenges of certain applications and therefore multi-component colloidal nanoparticle systems, such as ITO-ZnO [30], have received increasing attention, offering tailored functionalities and additional synergistic properties from combining disparate components [30,31]. Nanoporosity and the use of multicomponent TCOs is often desirable for sensing applications owing to the availability of large surface areas and a separation of functions between the different components (e.g., one component may exhibit high reactivity towards a target substance, while the other more stable part serves as a transducer) [32,33]. In such systems, modifications are often confined to the interfacial region while the original characteristics of each individual component can be largely retained [34]. Controlled fabrication of nanometric multicomponent particle structures by tailored mixing at specific scales,

i.e. at the primary particle level, at the cluster level or at the aggregate level is significant, especially for designing task-specific functionalities and understanding the fundamental physics [30,31,35]. The desired interactions of the NPs also need to be preserved throughout any patterning and other manufacturing steps. However, these mixed materials and their processing are still relatively under-explored for the TCO systems, despite their technological importance and diversity in optical and electrical properties.

In this paper, for the first time, we report a fast, scalable and energy/material-efficient route to the fabrication of bi-component GZO-ITO NP thin film TCOs on glass, using a straightforward drop-casting step from the corresponding surfactant-free, aqueous NP dispersions and CO<sub>2</sub> laser sintering. The electrical resistivity, optical bandgap energy and near-infrared absorbance of the sintered thin films can be fine-tuned through compositional adjustment of the two components, thereby providing opportunities to balance performance and sustainability across a range of potential applications. Adopting the same CO<sub>2</sub> laser source, we also demonstrate a fast, *additive* patterning route for the fabrication of TCO thin film tracks and circuit patterns, enabled through selective laser ablation of a polyester masking tape followed by drop casting of the NP dispersions into the openings. The convenient laser processing of a tape, with suitable adhesion and chemical stability to create a mask, is representative of a range of patterning methodologies that could also be used such as photoresist patterning or inkjet printing. The material combinations, together with the flexible deposition, patterning and laser processing methods, demonstrate excellent design freedom, low-cost, large scale integration possibilities and may also be applicable to other TCO thin films systems.

## 2. Experimental

### 2.1. Nanoparticle dispersion preparation

ITO nanopowders (NanoTek, Alfa Aesar, US) and GZO nanopowders (Pazet GK-40, Hakusui Tech, Japan) were used as-received without further purification. Deionised (DI) water was employed as the dispersant for the preparation of all of the ITO, GZO and bi-component GZO-ITO NP suspensions unless specified otherwise. In some cases for the dispersion of pure GZO NPs, to improve the resulting coating quality for electrical resistivity and optical transmittance measurement, the initial pH of the DI water used to prepare the dispersion was pre-adjusted to 6 by the addition of a small amount of hydrochloric acid (HCl) solution (37%, Sigma Aldrich, UK). The preparation of the GZO-ITO nanoparticle suspensions (typical batch size: 25 mL) proceeded first with the dispersion of ITO nanopowders in DI water utilising a two-step agitation process that involved using a magnetic stirrer at 300 r.p.m. for 2 h and subsequent ultrasonic probe agitation in an ice-water bath for 15 min using a Bandelin Sonopuls Ultrasonic Homogenizer equipped with a VS70/T transducer operating at 50 W and 15 kHz. This was followed by GZO nanopowder addition and a repetition of the two-step agitation process. An effective initial dispersion of ITO was key to the stabilisation of the following GZO-ITO suspensions. A low solid content (0.1 wt%) was normally used.

The suspension pH was assessed using an Accumet AE150 pH Meter (Fisher Scientific, UK). The hydrodynamic particle size distribution (PSD) and zeta ( $\zeta$ ) potential of the suspensions were measured using Dynamic Light Scattering (DLS) in a Zetasizer Nano ZS system (Malvern Instruments, Malvern, UK). The single-mode intensity-weighted PSD from cumulant analysis was converted to a number-weighted distribution using the built-in Zetasizer software.

TCO thin films were deposited using the prepared dispersions by drop casting (0.2 mL dispersion per square centimetre of substrate unless otherwise noted) on horizontally positioned soda lime glass (SLG) substrates (Thermo Scientific, US) of 24 mm × 24 mm × 1 mm. The dispersion film was then dried using a hotplate at 95 °C in air for at least 10 min. Before use, the glass substrates were cleaned utilising a DI

water/isopropyl alcohol mixture (volume ratio: 9:1) in an ultrasonic bath at 40 °C for 60 min and subsequently rinsed with DI water.

## 2.2. CO<sub>2</sub> laser processing of thin films

A 10.6 μm wavelength, CO<sub>2</sub> Synrad continuous-wave laser marker system (100 W maximum output power) was employed to laser-sinter the as-dried NP thin film specimens. This was carried out either in air or under an argon (Ar) gas atmosphere, with the latter facilitated by overlaying the specimen with a Perspex box into which Ar was flowed and allowed to escape through an opening positioned directly above the sample, through which the laser beam was also able to pass and impinge on the NP film. Laser patterns were designed using the built-in Synrad WinMark software. The laser beam was controlled using a 2-axis galvanometer mirror scanning system and focused with a 370 mm F-Theta lens, producing a Gaussian beam distribution with a 1/e<sup>2</sup> beam diameter of 540 μm at focus. Process parameters were varied, such as laser power (15%–25% power), translation speeds (500 to 3000 mm/s), resolution (100 to 400 dpi) and the number of laser passes over the whole pattern. Laser power was measured using a Coherent LM200 Probe and LabMax meter.

## 2.3. Circuit patterning methods and electrical component attachment

To create circuit patterns a high infrared absorbance and low thermal conductivity polyester adhesive tape (Tesa®50600, 80 μm thickness) was used as a mask on the glass and patterned through ablation using the CO<sub>2</sub> laser to reveal the underlying substrate. The laser process parameters were optimised for different aspects of the patterns: component contact areas used raster scanning at 9.6 W (20% power), 650 mm/s and 500 dpi, and the tracks used wobble scanning at 7.2 W (15% power) and 1000 mm/s with a wobble thickness of 0.5 mm and wobble step size of 0.03 mm. Ultrasonic cleaning in DI water was used to remove any debris from the pattern formed by laser ablation. A 2 μm thick 64.1 at.% In NP thin film was deposited from a single drop casting (0.5 mL per square centimetre of substrate) of the corresponding GZO-ITO dispersions (0.1 wt% solid content) into the openings in the polymer film, followed by drying at 95 °C on a hotplate in air. The thin film patterns were laser sintered using the same CO<sub>2</sub> laser source after peeling off the tape. For this step the laser was raster scanned across the entire area at 7.2 W (15% power), 1000 mm/s, 300 dpi and 2 laser passes under an Ar atmosphere, without causing noticeable damage to the exposed glass.

To attach the surface mount technology components, a commercial Ag-flake-filled conductive adhesive (EPO-TEK H20E) was stencil printed selectively onto the contact points of the TCO circuit pattern. The components were then placed manually and the entire assembly heated to 150 °C for 15 min on a hotplate in air to cure the adhesive and provide electrical and mechanical contact. The circuit was tested by applying a DC voltage of between 9 and 30 V at the relevant contact points.

## 2.4. Materials characterisation

Scanning electron microscopy (SEM) was employed in conjunction with Energy Dispersive X-ray (EDX) analysis to acquire microstructural and compositional information of the NP thin films using a JEOL 7800F FEGSEM fitted with an Oxford Instruments EDX detector. An in-situ lift-out method was used to prepare cross-sectional specimens for Transmission Electron Microscopy (TEM) analysis employing an FEI Helios PFIB Dual Beam Focused Ion Beam (FIB) system. This uses a xenon plasma as an ion milling source, rather than the Ga ion source used in a conventional FIB, thereby avoiding any interference of the composition during elemental analysis and Ga mapping. A platinum-carbon overlayer was deposited to define the surface and homogenise the final thinning of the specimens. TEM and High Resolution TEM

(HRTEM) images were acquired on a JEM-2100F (JEOL) and a FEI Tecnai F20, both of which were operated at 200 kV. The X-ray diffraction (XRD) analysis of the thin films was conducted using a Bruker D2 Phaser X-ray diffractometer, operating with a monochromatic Cu X-ray source ( $K_{\alpha} = 1.54184 \text{ \AA}$ ,  $K_{\beta}$  suppressed by a 0.5 mm thick nickel filter) along with 1 mm Divergence and 3 mm Anti-scatter slit widths.

For the surface morphology of the circuit and the cross-sectional microstructure/composition of the patterned thin films, the site-specific cross section was milled using a conventional dual-beam FEI Nova 600 Nanolab SEM fitted with an EDX detector. This cross section was gallium ion milled using an ion beam current reduced stepwise from 20 nA down to 300 pA, operating at 30 kV accelerating voltage. In this case, the intention was to observe the interconnection integrity of the conductive adhesive/TCO thin film/glass layers for which any Ga<sup>+</sup> implantation from the FIB Ga ion source was not expected to alter the microstructure.

## 2.5. Electrical and optical measurements

The DC resistivity ( $\Omega \cdot \text{cm}$ ) of the thin films on the insulating glass substrate was calculated as the product of sheet resistance ( $\Omega/\square$ ) and thin film thickness (cm). The thin film thickness was estimated through SEM observation of the fractured cross-sections, while the sheet resistance was measured using a 4-point probe fitted to a Keithley 2400 source-meter. The transmission and bandgap energy measurements were carried out using a Varian Cary UV-Vis 5000 spectrophotometer. The bandgap energy was estimated through a graphical extrapolation using the Tauc method [36].

## 3. Results and discussion

### 3.1. GZO-ITO bi-component dispersion characterisation

Due to the different stoichiometry and doping of ITO (Sn-doped In<sub>2</sub>O<sub>3</sub>) and GZO (Ga-doped ZnO), two notations are used in this paper to emphasise the relative proportions and total amount of materials in use. The atomic percentage (at.%) of the major metal cation In (from ITO) relative to Zn (from GZO) in the dispersion and thin film compositions is the primary method used throughout this paper to highlight the amount of In in the mixtures. In the following sections, the thin film compositions are based on the EDX analysis data, while the In content of the dispersions are based on the initial formulations. For ease of comparison, the weight percentage (wt%) of ITO to GZO is also presented alongside the atomic percentage where noted.

For aqueous dispersions of GZO-ITO nanoparticles at 0.1 wt% concentration, the effect of the suspension constituent compositions on the hydrodynamic particle size distribution (PSD), zeta ( $\zeta$ ) potential and drop cast thin film compositions are depicted in Fig. 1. A low solid content (0.1 wt%) was used for enhanced electrostatic repulsion resulting from the less compressed electric double layer compared with that obtained with relatively high solid content dispersions [37]. The as-dispersed pure GZO saw a  $\zeta$  potential of +6.2 mV at a pH of 8.8 with a mean particle size of 442.6 nm. When metal (M) oxides such as ZnO are dispersed in water, their surface tends to form a hydroxide layer ( $\equiv \text{M}-\text{OH}$ ) with a solubility mediated by the solution pH [38]. In the case of pure GZO dispersions, the slightly positive surface charge density is presumably due to surface protonation of the particle surface [39] as exemplified in Eq. (1).



The small magnitude of the  $\zeta$  potential resulted in a large mean particle size of 442.6 nm, which suggests that the ZnO-based NPs are susceptible to forming hard agglomerates in water [40]. Attempts were made to adjust the  $\zeta$  potential by changing the pH across the isoelectric point (pH: -9.3–9.7) through additions of diluted aqueous HCl or NaOH



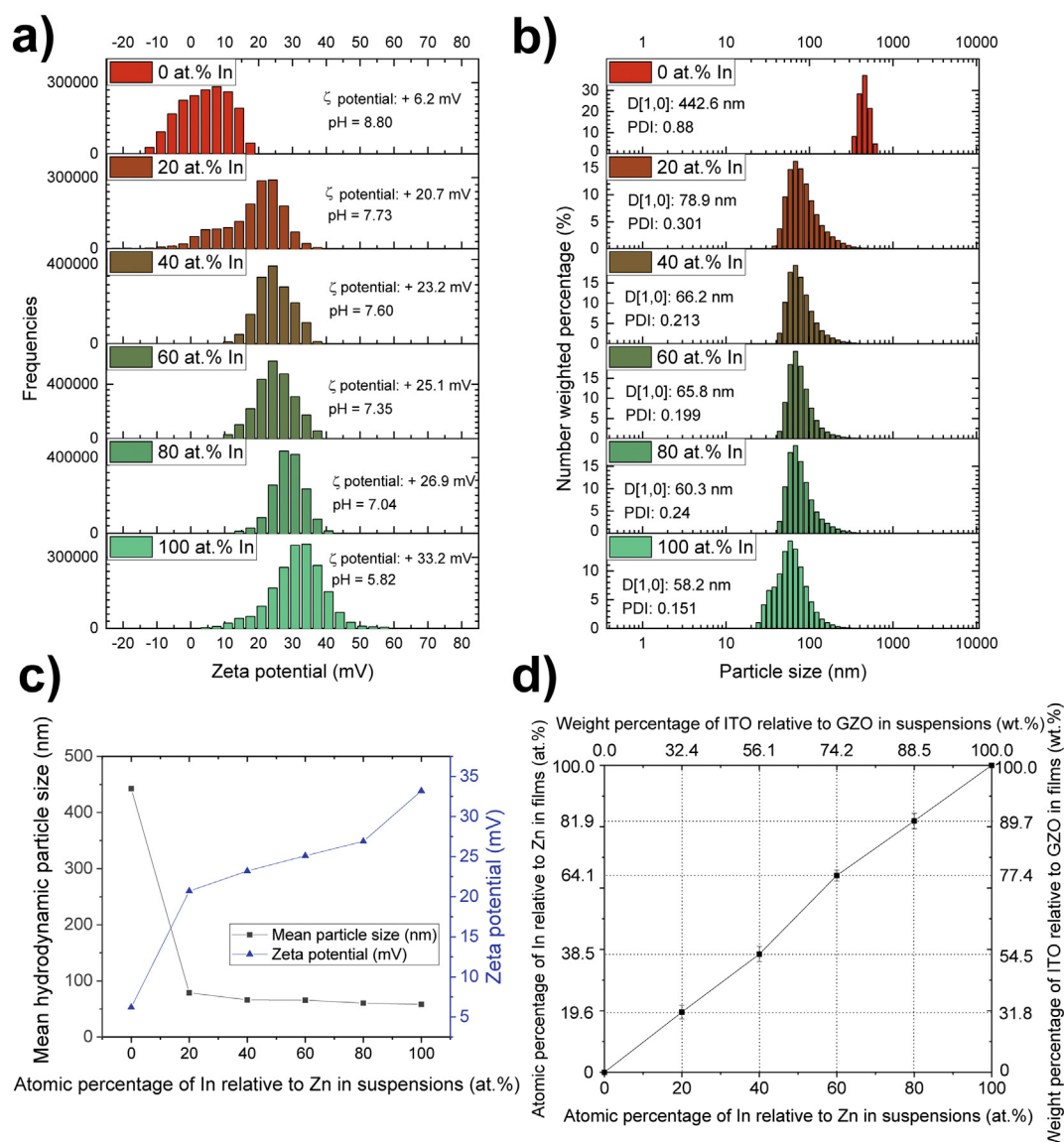


**Fig. 1.** Characterisation of the GZO-ITO aqueous dispersions. (a) zeta potential, (b) hydrodynamic particle size distribution (PSD), (c) plotted mean hydrodynamic particle size and suspension zeta potential, and (d) plotted atomic percentage of In (relative to Zn) and weight percentage of ITO (relative to GZO) in the resulting thin films, as a function of suspension constituent composition.

solutions. Suspension pH values  $<7.2$  and  $>12$  were found to give  $\zeta$  potentials with magnitudes in excess of 30 mV, indicative of improved dispersion stability, however only circumneutral conditions ( $6.6 < \text{pH} < 7.2$ ) were used in further trials to reduce the dissolution of GZO at low pH and minimise hydroxide formation [37] at high pH ( $>9$ ).

In contrast to GZO, the pure ITO dispersions had a resultant pH of 5.82 and a  $\zeta$  potential of +33.2 mV that led to an average hydrodynamic particle size of 58.2 nm. Upon water dispersion, the ITO NPs are thought to promote the release of protons that lower the pH. When GZO NPs were added to the ITO dispersion, the behaviour of the resultant suspension did not follow a simple linear rule of mixtures. An addition of as little as 20 at.% In relative to Zn (i.e. 32.4 wt% ITO relative to GZO NPs) adjusted the  $\zeta$  potential to +20.7 mV and significantly reduced and narrowed the particle size and its distribution. As shown in Fig. 1c, with increasing levels of ITO, the  $\zeta$  potential became more positive and the particle size decreased further, along with a reduction in the suspension pH, towards the levels of pure ITO dispersions. From the perspective of dispersion stabilisation, the addition of ITO NPs into GZO NP dispersions leads to two effects: first, the pH is reduced following a

release of protons, this helps to move the GZO NP system further from the isoelectric point and increase its  $\zeta$  potential. Second, the inherently more positively charged ITO NPs may enhance the electrostatic repulsion between the less positively charged GZO NPs through charge regulation resulting from a shift of the ion adsorption equilibrium upon particle approach, as described by the Poisson-Boltzmann (PB) model [41]. It was noted that the composition of the resultant thin films derived from the EDX area analyses (Fig. 1d) was comparable with the dispersion compositions, implying that there was no segregation or precipitation of individual components and a high degree of dispersion of the bi-component NP suspensions.

A TEM examination of the 20 at.% ITO NP suspension (further diluted to 0.005 wt% with water) drop-cast and dried on a carbon support film at 20 °C in air is shown in Fig. 2. The bi-component NP mixtures demonstrated an average primary particle size of 28.8 nm, which is lower than that acquired from the dynamic light scattering study (i.e. 78.9 nm). This is largely attributable to the latter method showing a hydrodynamic projection of clusters and agglomerates consisting of several NPs [42]. Some of the NPs displayed grouping into a randomly arranged

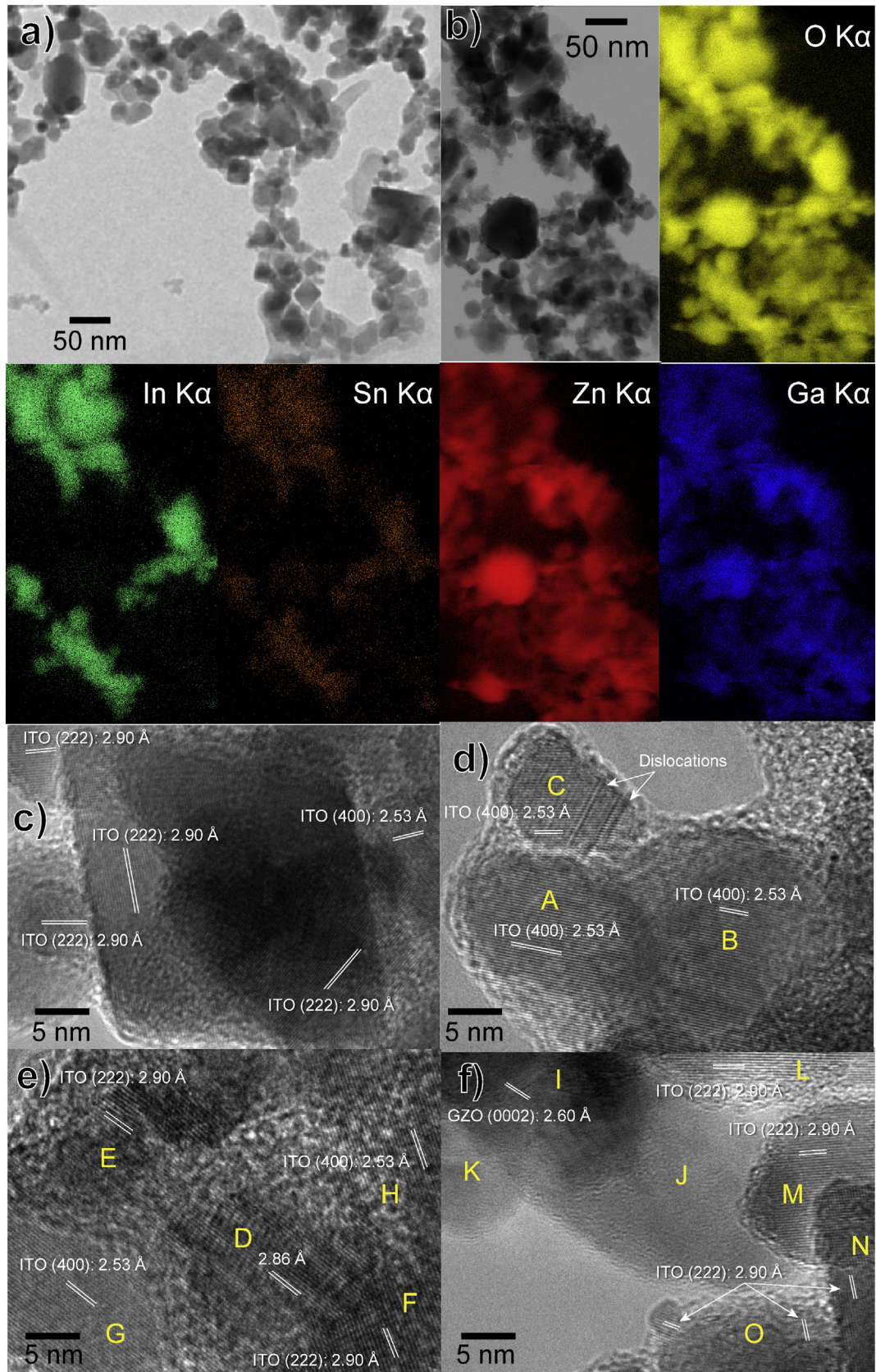


**Fig. 2.** Representative TEM images of a drop-cast, bi-component 20 at.% In-80 at.% Zn (32.4 wt% ITO-67.6 wt% GZO) NP dispersion. (a–b) Bright field images illustrating the grouping of NPs into chains and corresponding X-ray elemental maps of O, In, Sn, Zn and Ga obtained from the region shown in image (b). (c–f) HRTEM images of neighbouring NPs (labels A–H and L–O indicate ITO NPs, while I–K indicate GZO NPs).



chain format (Fig. 2a–b), pointing to the possibility of oriented attachment [43]. The attachment might have occurred during and/or before water evaporation, which increased the collision probability of the NPs as their concentration increased, together with an increasing compression of the electric double layer giving rise to decreasing electrostatic repulsion [37]. In Fig. 2b, the X-ray maps of O, In, Sn, Zn and Ga for the bi-component NP mixtures are presented. The NPs showing elevation of In and Sn content from ITO are clearly distinguished from those enriched with Zn and Ga that correspond to GZO, indicating that the two components largely retained their respective compositions. The GZO particles as the primary constituent appear throughout the X-ray maps, however the ITO NPs were not uniformly dispersed and were often found grouped into separate, high aspect-ratio clusters, which were assembled to form chain-like aggregates. HRTEM images (Fig. 2c–f) show that, albeit as a minor constituent (20 at.%), the cubic-phased ITO NPs (indexed with reference to JCPDS No. 06–0416  $\text{In}_2\text{O}_3$ ) were observed to predominantly demonstrate lattice fringes, indicative of high crystallinity [44]. Fig. 2c presents a case where the adjacent ITO NPs shared identical or similar (i.e. (222) and (400)) orientations but did not necessarily exhibit lattice fringe matching (i.e. the alignment and merging of the lattice fringes). Fig. 2d, however, presents a scenario where ITO particle A had aligned its (400) plane parallel to the (400) plane of ITO particle B, implying particle realignment. Also, ITO particle C in contact with A and B appeared to be undergoing realignment of its [400] direction with respect to particle B, presumably mediated by the observed intra-particle dislocation glides [45]. Fig. 2e depicts a probable ongoing merging process of adjacent ITO particles, where particle D, surrounded by particles at two inter-planar distances of 2.90 Å (E & F) and 2.53 Å (G & H), exhibited an intermediate d-spacing at 2.86 Å. This implies particle D might have been undergoing realignment through a structural relaxation process where the interplanar spacing slightly changed to adapt to its neighbouring particles [45,46]. On the other hand, adjacent GZO NPs were usually observed *not* to share similar crystal orientations. For instance, in Fig. 2f, the (0002) zone-axis for GZO particle I (indexed with reference to JCPDS No.79–0207 ZnO) did not coincide with those of the surrounding GZO particles J and K, as the latter two did not display any lattice fringes. This is in contrast with the ITO particles L–O in the same proximity which showed (222) orientations. Therefore, it appears that the segment formation of the bi-component NPs was evident before any deliberate sintering event, with the ITO NPs observed to demonstrate predominantly oriented attachment.

### 3.2. Laser sintering of GZO-ITO bi-component thin films

Thin films of the dispersions deposited by drop casting were  $\text{CO}_2$  laser-treated using a range of process parameters. The range of parameters investigated to optimise the laser treatment of approximately 800 nm thick pure ITO NP coatings for minimal electrical resistivity with respect to raster scanning speed and resolution can be found in the Supplementary Information Fig. S1. An argon (Ar) gas atmosphere was used to reduce the oxygen level around the sample during laser sintering and subsequent cooling. An inert atmosphere during sintering has been reported to facilitate the removal of carrier-trapping interstitial oxygen, thereby increasing the free carrier concentration of TCO materials [27]. The laser process windows were governed by sufficient energy input to facilitate NP sintering, while minimising overheating that would otherwise instigate coating cracking and delamination [47] as well as damage the underlying glass substrate. With a scanning velocity in between 500 and 3000 mm/s and a resolution in between 100 and 400 dpi, the lowest resistivity for pure ITO was  $7.34 \times 10^{-3} \Omega \cdot \text{cm}$ , located at 1000 mm/s and 300 dpi, for an optimised power input of 7.2 W and two passes of the laser over the surface. The lowest resistivity reported in this study is comparable, if not lower than those of studies concerning the heat treatment of pure ITO NP thin films, typically in the range of  $10^{-1}$  to  $10^{-3} \Omega \cdot \text{cm}$  [6,26,29,48]. Similar trends in the

dependence of resistivity on the scanning velocity and resolution were observed for the GZO-ITO mixtures, indicative of the predominant role of the more conductive ITO phase in contributing to the overall conduction. The optimal laser treatment conditions identified for pure ITO were therefore applied to the other compositions.

Fig. 3 shows the representative surface morphology, elemental mapping and X-ray diffractograms of various NP coating compositions following drop casting on glass, ambient drying at 95 °C and  $\text{CO}_2$  selective laser sintering at the optimal condition (i.e. 7.2 W, 1 m/s translation speed, 300 dpi resolution, 2 laser passes). The addition of 19.6 at.% In (i.e. 31.8 wt% ITO) substantially improved the coating surface morphology from a discrete, spongy distribution of micron-sized agglomerates of GZO NPs, into a continuous, nanoporous structure enriched in GZO NPs. The improved coating morphology was retained as the co-deposited ITO content increased up to 100 at.% In. The thin film morphology through the drop casting was comparable to those obtained through wet deposition methods such as spin coating of nanoparticle suspensions [26], however the present method offers near-zero-loss material usage. Low voltage EDX mapping (at 5 keV) was conducted to gain a spatially resolved insight [49] into the bi-component GZO-ITO phase distribution at the coating surface. The interaction volume was estimated as 0.15  $\mu\text{m}$  for ITO and 0.17  $\mu\text{m}$  for GZO based on a Monte Carlo simulation using the Casino software [50]. The In  $L\alpha$  line was used as a marker for ITO and the Zn  $K\alpha$  line was used for GZO. All the ITO-containing compositions down to 19.6 at.% In saw a relatively homogeneous distribution of ITO, whereas the low GZO compositions, e.g. 64.1 at.% In and 81.9 at.% In, displayed the discrete presence of agglomerated clusters of GZO NPs up to submicron size. This suggests the mean size of the ITO NP clusters was smaller than that of the GZO NP clusters. XRD patterns shown in Fig. 3 indicate that the hybrid coatings consisted of a mixture of hexagonal-phased gallium-doped zinc oxide and cubic-phased tin-doped indium oxide, without any new reaction product arising from the laser sintering process. This indicates the preservation of the intrinsic characteristics of the two individual TCO components throughout the sintering.

The DC electrical resistivity, optical transmittance and optical bandgap energy of approximately 800 nm-thick, laser sintered TCO thin films are presented in Fig. 4. For the preparation of the pure GZO film for optical and electrical characterisation, DI water with pH initially adjusted to 6 (through addition of HCl solution) was employed as the dispersant. This pH was chosen as it was similar to that obtained for the pure ITO dispersions and decreased the mean hydrodynamic particle size of the GZO NP suspension from 442.6 nm (i.e. dispersed with DI water only) to 131.6 nm, while also improving the drop-cast coating uniformity at low solid contents (i.e. 0.1 wt%) from that depicted in Fig. 3 to that shown in Fig. 4b. Fig. 4a shows the variation in resistivity as a function of ITO composition, for which it was found that using Ar in place of air as the laser sintering atmosphere induced a systematic reduction in the resistivity that was particularly significant for the ITO-containing samples. The pure GZO coating laser-treated under Ar showed a resistivity around 116  $\Omega \cdot \text{cm}$ , but with an increase in the co-deposited ITO content from 0 to 19.6 at.% In, there was a substantial reduction to 0.32  $\Omega \cdot \text{cm}$ , signifying the predominant role of the ITO content in contributing to electrical conduction. Further increasing the co-deposited ITO content up to 100 at.% In gave a largely logarithmic reduction in resistivity, culminating at  $7.34 \times 10^{-3} \Omega \cdot \text{cm}$  for 100 at.% In.

For the optical transmittance derived from UV-vis spectroscopy, it was found that despite a thin film thickness of 800 nm, most of the GZO-ITO compositions exhibited a transmittance close to or exceeding 75% in the visible region. The coatings also demonstrated decreasing near-infrared (i.e. 800–1500 nm wavelength) transmittance with increasing ITO content due to the high carrier concentration of the ITO component, giving rise to pronounced free carrier absorption [51]. The SLG substrates exhibited good visible-range transmittance with the major loss due to reflectance that was thought to have a minimal masking effect on the visible-range transmittance of the TCO thin

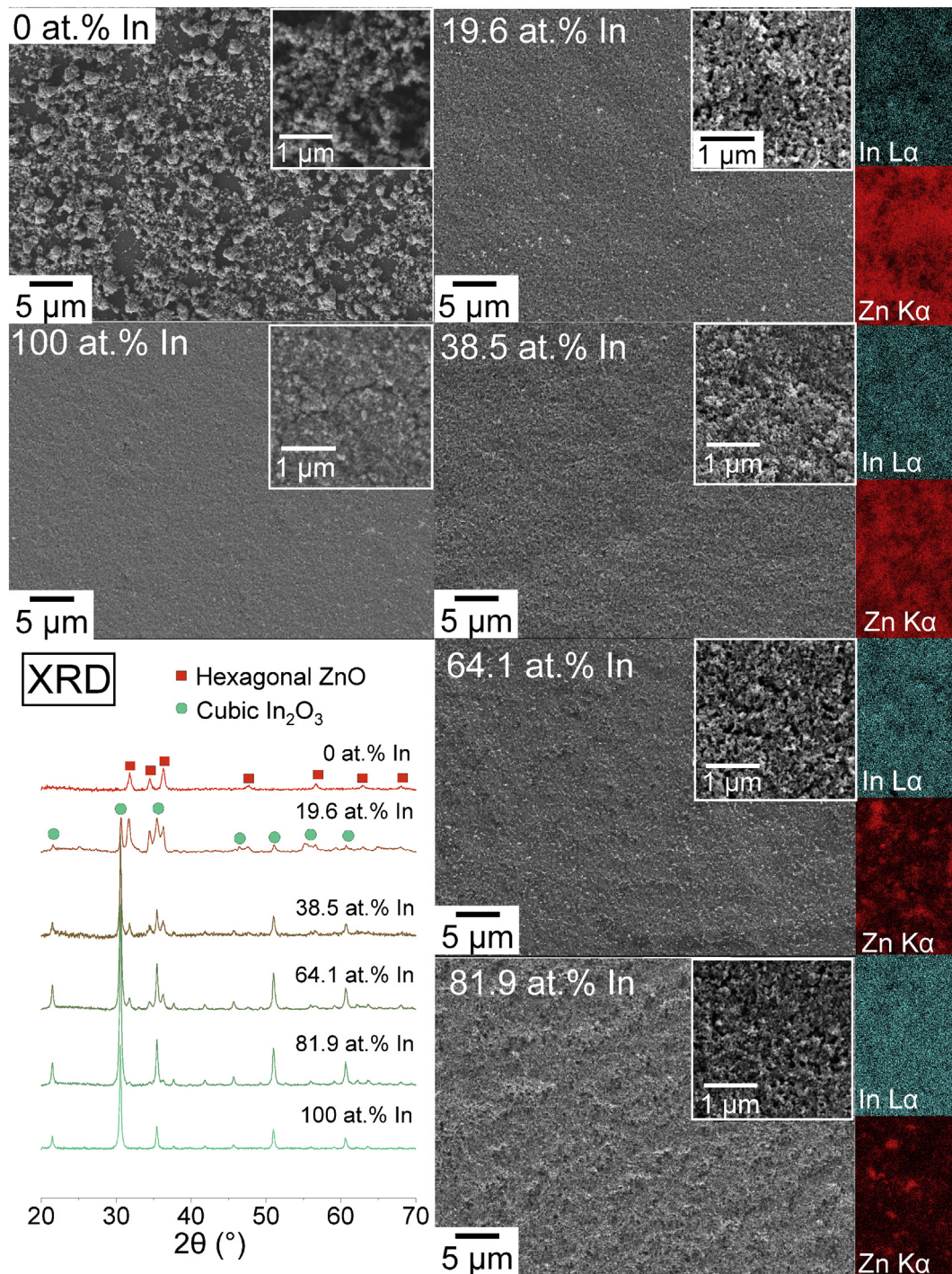


**Fig. 3.** SEM images, corresponding 5 keV X-ray maps of In and Zn (obtained from inset image areas) and XRD patterns for approximately 800 nm thick, bi-component GZO-ITO NP coatings as a function of constituent film composition in at.% of In (relative to Zn). All samples were laser-treated under Ar at 7.2 W power, 1 m/s translation speed, 300 dpi resolution and with 2 laser passes.

films. The direct optical bandgap energy derived from Tauc plots (Fig. 4d) showed compositionally dependent variations between 3.33 eV for pure GZO (0 at.% In) and 3.93 eV for pure ITO (100 at.% In). In the case of pure GZO (0 at.% In), a step increase in the slope of the Tauc plot was also observed at ca. 3.9 eV, which can be ascribed to the less uniform structure of these coatings, due to poor NP dispersion, such that thickness variation across the specimen led to a contribution from the underlying SLG substrate (optical band gap energy measured

as 4.2 eV). It is interesting that the Tauc plots for the bi-component films do not appear to show steps that might be associated with the separate band gap energies of the two components. Instead for these mixed GZO-ITO NP films, the estimated optical bandgap energy appears to derive collectively from the absorption of the two individual TCO phases arising from their respective interband transitions. This therefore demonstrates a tuning capability of the optical bandgap energy with film composition to suit various applications [51].



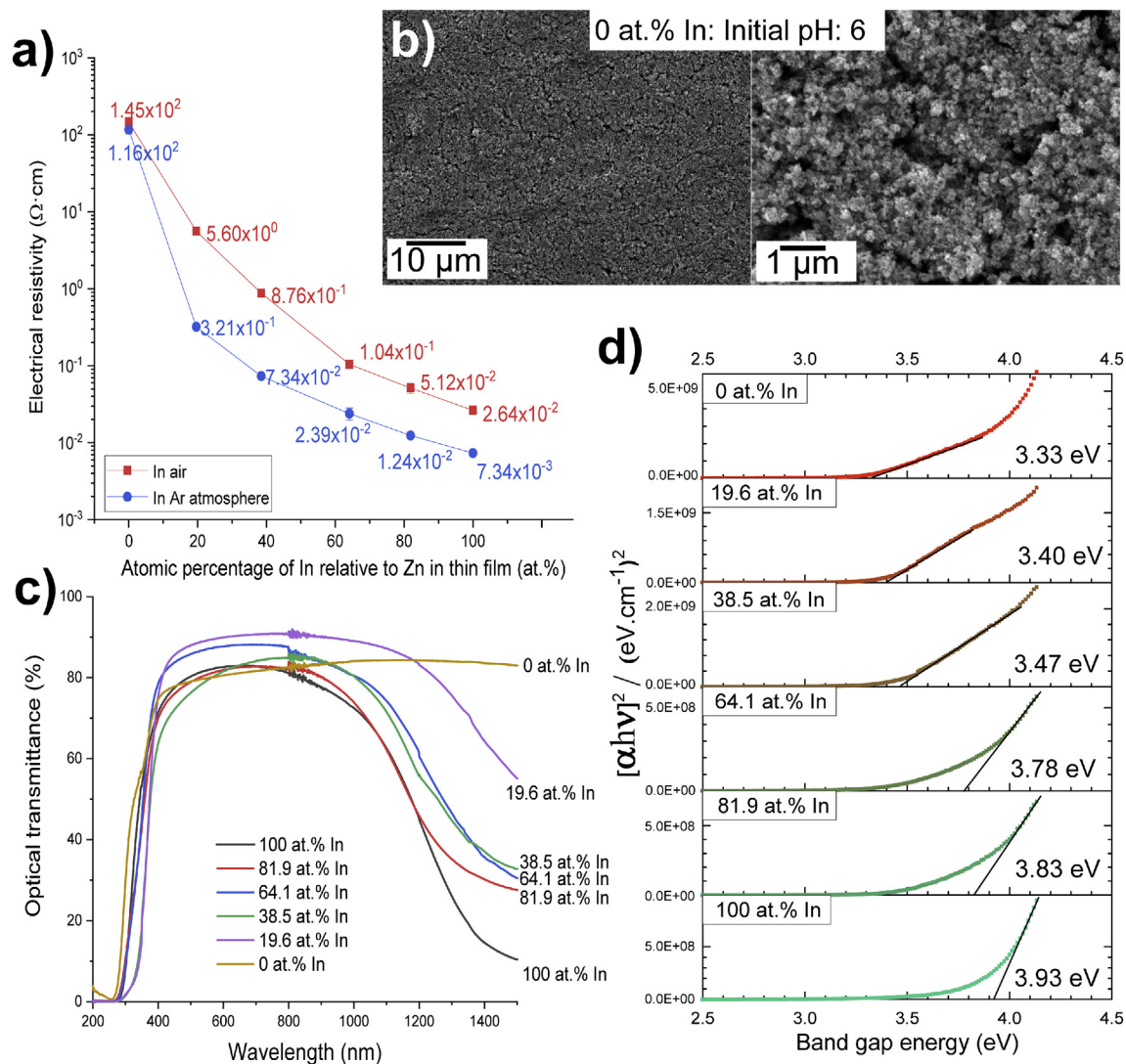


**Fig. 4.** Electrical and optical property assessment as a function of at.% In content of 800 nm thick, laser-sintered, bi-component GZO-ITO thin films. (a) Electrical resistivity derived from sheet resistance measurements, (b) SEM images showing the improved surface morphology of a pure GZO NP coating (prepared from DI water with an initial pH of 6) used for electrical resistivity and optical transmittance measurement; (c) optical transmittance, and (d) estimated optical bandgap energy.

### 3.3. Self-assembly of ITO NPs through oriented attachment and its implications for electrical conduction

In order to understand the phase distribution and sintering characteristics of the bi-component NP coating, a combined High-Angle Annular Dark-Field (HAADF)/HRTEM examination was conducted on the cross-section of a laser-sintered (using the optimised process conditions), approximately 2  $\mu\text{m}$  thick, bi-component 19.6 at.% In–80.4 at.% Zn coating on a glass substrate. A standard TEM specimen lift-out was adopted using a gallium-free, Xenon Plasma Focused Ion Beam (P-FIB) system. Fig. 5a presents an overview of the cross-sectional microstructure, which appeared continuous and nanoporous with an intact coating/glass interface. HAADF imaging at higher magnifications (Fig. 5b–c) points to the universal presence of oriented-attached ITO NP chains. The ITO NPs have a higher average atomic number (ca. 24) compared with that of the GZO NPs (ca. 17.8) and therefore appear lighter in contrast due to increased high-angle incoherent electron scattering [52]. In Fig. 5b, the randomly arranged ITO NP chains formed a scaffold-like network with extensive bridging. Fig. 5c shows the grouping of ITO NPs into an irregular chain geometry. Fig. 5d–f provide representative HRTEM images of the sintered microstructures of the bi-component NP coatings. Fig. 5d depicts evident necking phenomena between

three ITO particles defined by two distinct grain boundaries. The lattice fringes, complicated with pronounced moiré fringes caused by overlapping nanocrystals in the electron beam direction, suggest that the particles exhibited varying d-spacing, e.g. 4.17 Å and 4.27 Å for the (211) orientation. This signifies the particle merging had involved gradual structural relaxation [45]. Fig. 5e shows a sintered ITO grain with an in-plane size exceeding 100 nm, displaying a unifying (222) orientation across the grain structure, yet with discontinuity in the lattice fringes implying a merging history of several ITO particles. A GZO (10 $\bar{1}$ 1) particle was observed in contact with the ITO grain, yet not necessarily exhibiting aligned orientations. Fig. 5f shows a collection of adjacent GZO grains (particles) which shared similar orientations of (0002). Again, the ITO particle in proximity did not seem to share lattice fringe matching or demonstrate clear interfaces with the GZO particles.

Fig. 6 suggests a mechanism for the formation and structure of the bi-component ITO-GZO thin films. As indicated by the TEM images of drop-cast samples shown in Fig. 2, adjacent ITO NPs in the suspension are thought to be already partially self-assembled through sharing specific crystallographic orientations and particle docking at interfaces, giving rise to a phenomenon often referred to as ‘oriented attachment’ or ‘contact epitaxy’ [53]. This is thought to be thermodynamically driven by an elimination of the pairs of high energy surface facets upon particle

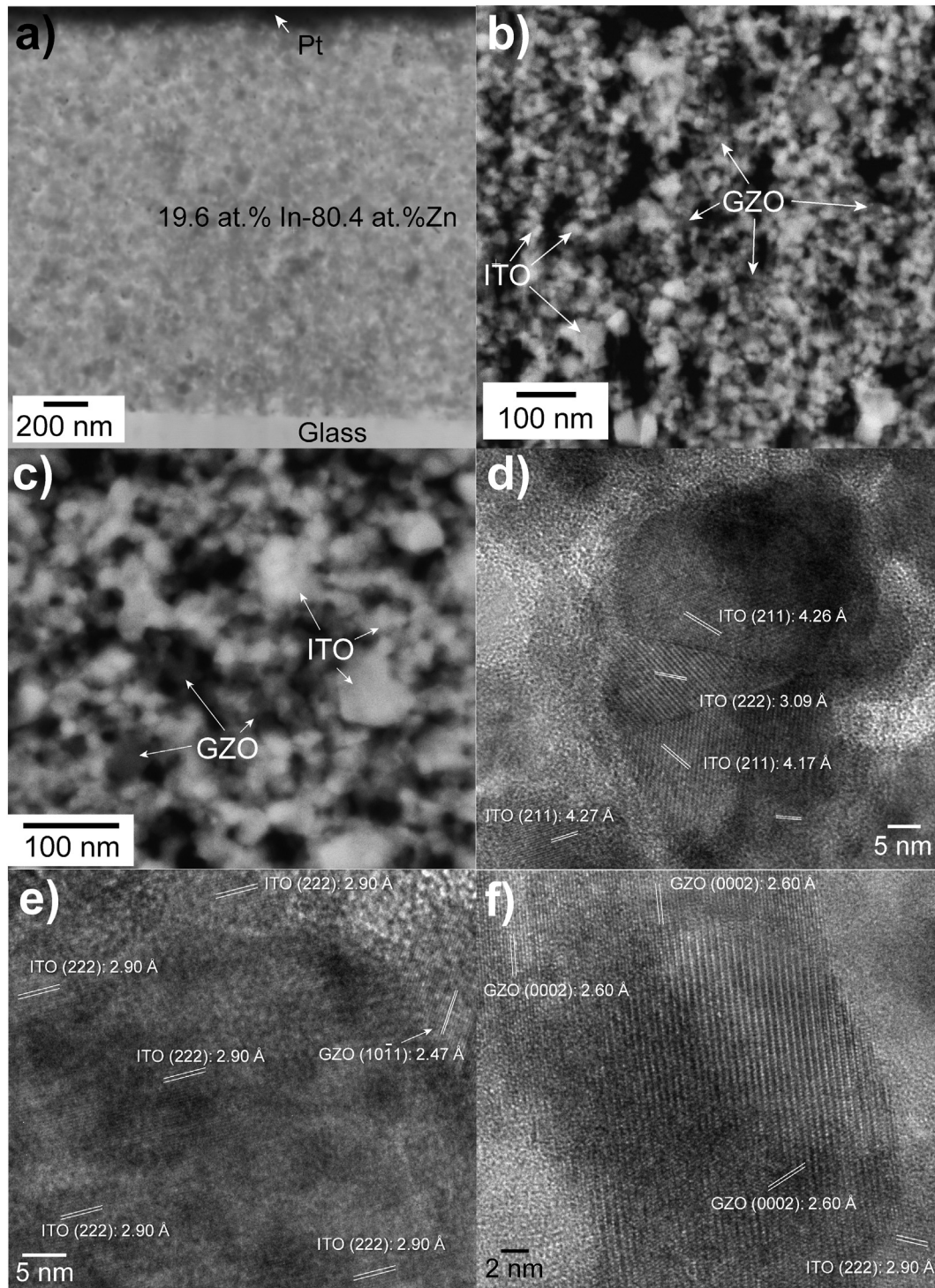


**Fig. 5.** (a) Representative TEM bright field image, (b–c) High-Angle Annular Dark-Field (HAADF) TEM images, and (d–f) HRTEM images of the cross-section of a laser-sintered 19.6 at.% In-80.4 at.% Zn coating on a glass substrate.

contact, which leads to a significant reduction in the surface free energy [54,55]. For dispersion of the dissimilar NPs, we did not use any organic dispersant or surfactant primarily for three reasons. First, it is environmentally appealing to have a process system which in addition to the two TCO NP materials contains only water. Second, the enhanced electrostatic repulsion rendered by the ITO NP addition into the GZO system circumvented the necessity of a dispersant. Finally, the presence of an organic capping agent could hinder the desirable oriented attachment between NPs and would also require a prolonged burn-out process prior to laser sintering.

In electrically conductive composites, conductive filler particles are typically added into an insulating, e.g. polymer matrix, in sufficient quantity (above the percolation threshold) to enable a long range network of low resistance contacts and pathways [56,57]. In this study the relatively low conductivity GZO particles can be considered a nanoporous matrix, however with only a 19.6 at.% addition of ITO the resistivity of the resulting film decreased by a factor of 361. The formation of ITO NP segments during the dispersion stage is thought to be retained when the suspension is deposited and dried on the glass substrate and subsequently laser processed. The present system is,



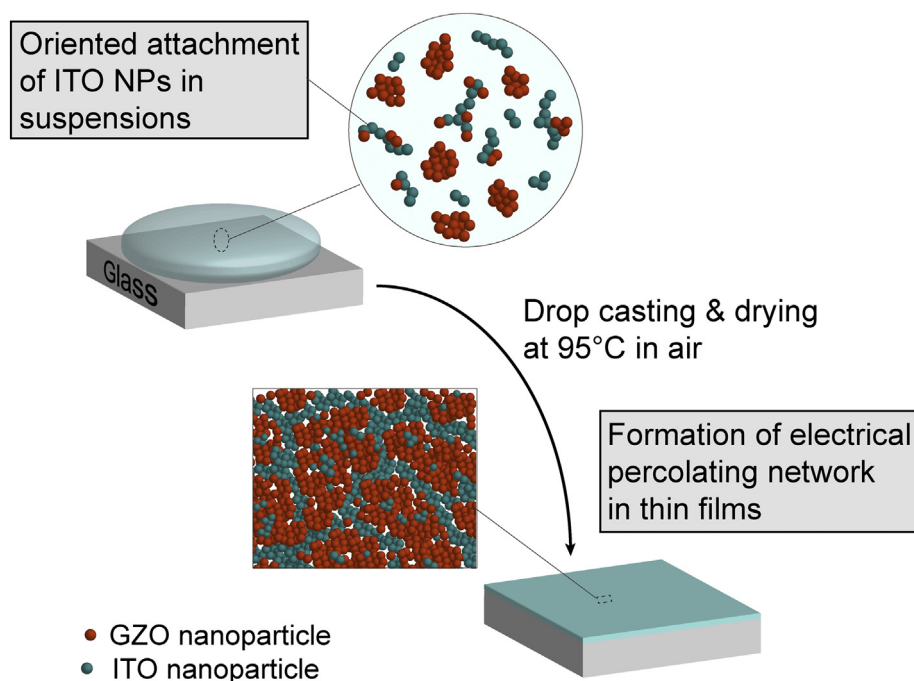


Fig. 6. Schematic diagrams depicting the self-assembly of the bi-component GZO-ITO NPs in suspension and the deposition of a bi-component NP thin film through a drop casting route.

therefore, considered to constrain high aspect-ratio groups of ITO NPs with self-avoiding walk (SAW) conformations as the percolating units within a matrix of nanoporous GZO. When treated within a simple 2-D square lattice, the variations of the percolation threshold,  $p_c$ , with the segment length  $L_c$  has been suggested [58] to demonstrate a power-law decay following Eq. (2):

$$p_c \propto L_c^{-0.1} \quad (2)$$

This suggests that an increase in the length of the percolating unit, e.g. through transformation of the geometry from small ellipsoidal clusters of NPs that are tens of nanometers in size into high aspect-ratio chain segments, effectively lowers the electrical percolation threshold [56,59] and aids in the establishment of long-range connectivity [60].

#### 3.4. Patterning of bi-component NP deposits to form circuit tracks

The feasibility of applying the bi-component TCO NP materials as patterned transparent tracks for a surface mount technology Light Emitting Diode (LED) circuit on a glass substrate is demonstrated in Fig. 7, using a bi-component 64.1 at.% In thin film. A schematic diagram depicting the process flow is also presented, together with representative SEM/EDX analysis data showing the surface and cross-sectional microstructure of the assembled component interconnects and TCO tracks. Upon drop casting, the laser-machined openings in the polymer tape were found to be effective in holding a reservoir of the NP dispersions, giving rise to fast build-up of the film thickness when dried. The laser sintering of the NP films could then be performed, after tape removal, by raster scanning the beam across the entire sample using the optimised parameters identified for TCO sintering. An example of the patterned track sample is given in the photograph inset demonstrating the optical transparency. From SEM imaging, the thin film tracks were found to be continuous in structure, without any evident cracking or delamination. The optimal transmittance and conductivity of these tracks were also retained compared with their un-patterned thin film counterparts. From the FIB cross-section microstructural analysis, the bi-component TCO tracks showed a cross-sectional area of approx.

$2 \mu\text{m} \times 500 \mu\text{m}$  and intact interfaces with both the overlying Ag-flake conductive adhesive and underlying glass substrate. When the power terminals were connected to a 30 V DC power supply, the LED illuminated, indicative of the establishment of the long-range connectivity across the substrate surface. The circuit was not fully functional as the LED did not flash, which is thought to be due to the higher resistance of the tracks compared to the equivalent thicker and more conductive copper tracks for which the circuit was originally designed to operate at <10 V. However, this demonstrates the potential of this route to create optically transparent circuit patterns that could be designed in the future with increased overall track thickness/width to achieve the desired performance.

#### 4. Conclusions

In this study, we introduced a fast, scalable and material/energy-efficient processing route to fabricate bi-component GZO-ITO thin films and tracks from NP suspensions in order to reduce the amount of ITO required to form these electrically conductive structures. Some conclusions can be drawn as follows:

- 1) An aqueous dispersion of ITO NPs (down to 20 at.% In relative to Zn from GZO) was found to stabilise GZO NPs through the release of protons and electrostatic repulsion provided by the ITO NPs. This increased the magnitude of the average zeta potential, reduced the mean hydrodynamic particle size in the suspension and circumvented the need for any organic surfactant or dispersant. High-aspect ratio cluster (chain segment) formation of ITO NPs through oriented attachment was observed in TEM investigations and these are thought to create an electrical percolating network within a less conductive GZO NP matrix when forming thin films. Further work could focus on using Small Angle Scattering-based techniques to probe the hierarchical structuring of the NP clusters in the suspension.
- 2) The rapid  $\text{CO}_2$  laser sintering of approximately 800 nm thick NP films under Ar gas yielded resistivities of  $7.34 \times 10^{-3} \Omega \cdot \text{cm}$  for pure ITO and  $116 \Omega \cdot \text{cm}$  for pure GZO, with their bi-component mixtures showing a non-linear dependence of resistivity on the composition.



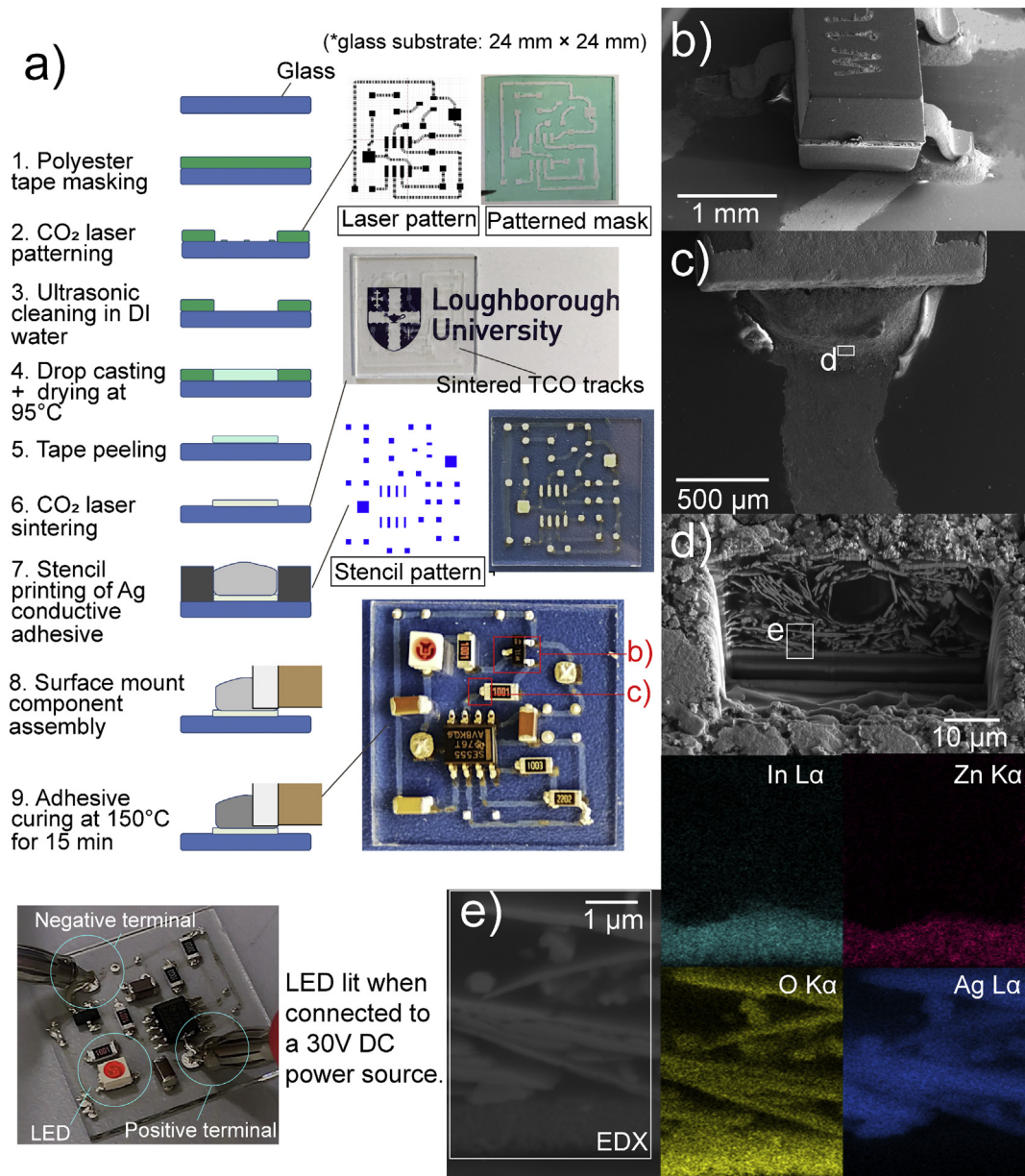


**Fig. 7.** Development of a fast laser patterning and sintering process route for the fabrication of 64.1 at.% In NP thin film tracks on glass, with the demonstration of a surface mount LED circuit assembled with a commercial Ag filled conductive adhesive. (a) Process flow of the circuit patterning and assembly, (b) SEM image of the connection between a component and track, (c) overview of a component interconnect indicating the area analysed by FIB, (the analysis locations of both (b) and (c) are indicated in the photograph of the assembled LED circuit in (a)) (d) SEM image of a FIB cross-section into the interconnect with an indication of the area analysed by EDX, (e) high magnification SEM image of the FIB cross-section and associated EDX element maps.

An addition of 19.6 at.% ITO lowered the DC resistivity of the GZO-based films by a factor of 361, which further decreased with increasing co-deposited ITO content. This was accompanied by decreasing optical transmittance in the near-infrared region and increasing optical bandgap energy (from 3.33 eV for pure GZO to 3.93 eV for pure ITO), along with >75% transmittance in the visible region for all the composition variations studied. This allows for fine-tuning and design of films and structures with controlled electrical and optical properties through compositional adjustment, without compromising the original characteristics of the two individual TCO components.

- 3) Lastly, using three straightforward process steps: the CO<sub>2</sub> laser patterning of a mask, the drop casting of NP suspensions into the mask openings and CO<sub>2</sub> laser sintering of the NP thin films, the feasibility of forming bi-component NP transparent tracks for an LED

circuit was demonstrated on a glass substrate. The proposed patterning-deposition-sintering approach presents a rapid, material-efficient and energy-efficient route to the sustainable manufacture of TCO thin films with significant impact for applications where ITO cannot be effectively replaced.

Supplementary data to this article can be found online at <https://doi.org/10.1016/j.matdes.2020.108865>.

#### Data availability

The raw/processed data required to reproduce these findings are included in this article or are available from the corresponding author on request.

## CRediT authorship contribution statement

**Jing Wang:** Conceptualization, Methodology, Investigation, Writing - original draft. **Fabiana Lisco:** Methodology, Investigation, Writing - review & editing. **David A. Hutt:** Conceptualization, Methodology, Writing - review & editing, Supervision, Funding acquisition. **Lewis C.R. Jones:** Methodology, Writing - review & editing. **Jake W. Bowers:** Writing - review & editing, Supervision. **Patrick J.M. Isherwood:** Writing - review & editing, Supervision. **Zhaoxia Zhou:** Investigation, Writing - review & editing. **Paul P. Conway:** Supervision, Writing - review & editing, Funding acquisition.

## Declaration of competing interest

The authors declare that they have no known competing financial interests or personal relationships that could have appeared to influence the work reported in this paper.

## Acknowledgements

This research was funded by the UK Engineering and Physical Sciences Research Council (EPSRC) under grant number EP/L017709/1. The authors would like to thank David Britton, Loughborough University for the modification of the CO<sub>2</sub> laser apparatus and laser pattern optimisation. The authors acknowledge use of the facilities within the Loughborough Materials Characterisation Centre (LMCC) including access to the Helios PFIB, funded by EPSRC grant EP/P030599/1, and are grateful to Stuart Robertson, Ben Maerz, Scott Doak, Keith Yendall and Sam Davis of LMCC for their assistance with the specimen preparation and acquisition of Plasma-FIB, TEM and SEM data. We also wish to thank Michael Fay from the Nanoscale and Microscale Research Centre (NMRC), University of Nottingham, UK for the support of data acquisition on the JEOL-2100F TEM. The collaboration of the other academic project partners at Loughborough University and University College London is also gratefully acknowledged, together with the support of the industrial partners, especially Malvern Instruments, Ltd. (UK) for the provision of a Zetasizer Nano system for particle size and zeta potential analysis.

## References

- [1] S. Calnan, A.N. Tiwari, High mobility transparent conducting oxides for thin film solar cells, *Thin Solid Films* 518 (2010) 1839–1849, <https://doi.org/10.1016/j.tsf.2009.09.044>.
- [2] D.S. Ginley, C. Bright, Transparent conducting oxides, *MRS Bull.* 25 (2000) 15–18, <https://doi.org/10.1557/mrs2000.256>.
- [3] T. Minami, Transparent conducting oxide semiconductors for transparent electrodes, *Semicond. Sci. Technol.* 20 (2005) S35–S44, <https://doi.org/10.1088/0268-1242/20/4/004>.
- [4] A.N. Fouda, E.S.M. Duraia, Self-assembled graphene oxide on a photocatalytic active transparent conducting oxide, *Mater. Des.* 90 (2016) 284–290, <https://doi.org/10.1016/j.matdes.2015.10.139>.
- [5] V. Awasthi, V. Garg, B.S. Sengar, S.K. Pandey, Aaryashree, S. Kumar, C. Mukherjee, S. Mukherjee, Impact of sputter-instigated plasmonic features in TCO films: for ultrathin photovoltaic applications, *Appl. Phys. Lett.* 110 (2017) 103903–1–103903–5, <https://doi.org/10.1063/1.4978269>.
- [6] T.A. Nirmal Peiris, S. Ghanizadeh, D.S.Y. Jayathilake, D.A. Hutt, K.G.U. Wijayantha, P.P. Conway, D.J. Southee, I.P. Parkin, P. Marchand, J.A. Darr, C.J. Carmalt, Aerosol-assisted fabrication of tin-doped indium oxide ceramic thin films from nanoparticle suspensions, *J. Mater. Chem. C* 4 (2016) 5739–5746, <https://doi.org/10.1039/c6tc00812g>.
- [7] P. Chen, Z. Chen, S. Hou, X. Shen, Y. Chu, Y. Yang, L. Yang, J. Li, N. Dai, In-situ growth of highly monodisperse ITO nanoparticles regulated by mesoporous silica glasses, *Mater. Des.* 151 (2018) 53–59, <https://doi.org/10.1016/j.matdes.2018.04.036>.
- [8] Y.S. Liu, C.Y. Hsieh, Y.J. Wu, Y.S. Wei, P.M. Lee, H.M. Hsieh, C.Y. Liu, Mechanism of conductivity degradation of AZO thin film in high humidity ambient, *Appl. Surf. Sci.* 282 (2013) 32–37, <https://doi.org/10.1016/j.apsusc.2013.04.167>.
- [9] Y.N. Ahn, H. Yoon, S.H. Lee, H.H. Lee, H. Kim, Formation of randomly dispersed pores in Ga-doped ZnO between Al<sub>2</sub>O<sub>3</sub> and glass via promoted atomic diffusion: experimental and computational study, *Mater. Des.* 93 (2016) 304–310, <https://doi.org/10.1016/j.matdes.2015.12.133>.
- [10] S.H. Lee, S.H. Han, H.S. Jung, H. Shin, J. Lee, J.H. Noh, S. Lee, I.S. Cho, J.K. Lee, J. Kim, H. Shin, Al-doped ZnO thin film: a new transparent conducting layer for ZnO nanowire-based dye-sensitized solar cells, *J. Phys. Chem. C* 114 (2010) 7185–7189, <https://doi.org/10.1021/jp1008412>.
- [11] T. Dhakal, A.S. Nandur, R. Christian, P. Vasekar, S. Desu, C. Westgate, D.I. Koukis, D.J. Arenas, D.B. Tanner, Transmittance from visible to mid infra-red in AZO films grown by atomic layer deposition system, *Sol. Energy* 86 (2012) 1306–1312, <https://doi.org/10.1016/j.solener.2012.01.022>.
- [12] R. Matthews, E. Glasser, S.C. Sprawls, R.H. French, T.J. Peshek, E. Pentzer, I.T. Martin, Organofunctional silane modification of aluminum-doped zinc oxide surfaces as a route to stabilization, *ACS Appl. Mater. Interfaces* 9 (2017) 17620–17628, <https://doi.org/10.1021/acsami.7b02638>.
- [13] F. Iskandar, Nanoparticle processing for optical applications - a review, *Adv. Powder Technol.* 20 (2009) 283–292, <https://doi.org/10.1016/j.apt.2009.07.001>.
- [14] T. Nikolajsen, K. Leosson, S.I. Bozhevolnyi, Surface plasmon polariton based modulators and switches operating at telecom wavelengths, *Appl. Phys. Lett.* 85 (2004) 5833–5835, <https://doi.org/10.1063/1.1835997>.
- [15] S. Franzen, Surface plasmon polaritons and screened plasma absorption in indium tin oxide compared to silver and gold, *J. Phys. Chem. C* 112 (2008) 6027–6032, <https://doi.org/10.1021/jp7097813>.
- [16] K. Ellmer, A. Klein, B. Rech, Transparent conductive zinc oxide: Basics and applications in thin film solar cells, choice rev. online. 45, Springer Series in Materials Science, 104, Springer, 2008 <https://doi.org/10.5860/choice.45-6197>.
- [17] R.W. Crisp, M.G. Panthani, W.L. Rance, J.N. Duenow, P.A. Parilla, R. Callahan, M.S. Dabney, J.J. Berry, D.V. Talapin, J.M. Luther, Nanocrystal grain growth and device architectures for high-efficiency CdTe ink-based photovoltaics, *ACS Nano* 8 (2014) 9063–9072, <https://doi.org/10.1021/nn502442g>.
- [18] C.S. Anderson, U.S. Geological Survey Minerals Yearbook - 2016: Indium (Advance Release), 2019.
- [19] T. Minami, T. Miyata, T. Yamamoto, Work function of transparent conducting multi-component oxide thin films prepared by magnetron sputtering, *Surf. Coatings Technol.* 108–109 (1998) 583–587, [https://doi.org/10.1016/S0257-8972\(98\)00592-1](https://doi.org/10.1016/S0257-8972(98)00592-1).
- [20] M.J. Powell, D.B. Potter, R.L. Wilson, J.A. Darr, I.P. Parkin, C.J. Carmalt, Scaling aerosol assisted chemical vapour deposition: exploring the relationship between growth rate and film properties, *Mater. Des.* 129 (2017) 116–124, <https://doi.org/10.1016/j.matdes.2017.05.017>.
- [21] M. Gao, X. Wu, J. Liu, W. Liu, The effect of heating rate on the structural and electrical properties of sol-gel derived Al-doped ZnO films, *Appl. Surf. Sci.* 257 (2011) 6919–6922, <https://doi.org/10.1016/j.apsusc.2011.03.031>.
- [22] S.T. Zhang, J.L. Rouvière, V. Consonni, H. Roussel, E. Pernot, D. Muñoz-Rojas, A. Klein, D. Bellet, High quality epitaxial fluorine-doped SnO<sub>2</sub> films by ultrasonic spray pyrolysis: structural and physical property investigation, *Mater. Des.* 132 (2017) 518–525, <https://doi.org/10.1016/j.matdes.2017.07.037>.
- [23] H. Hagendorfer, K. Lienau, S. Nishiwaki, C.M. Fella, L. Kranz, A.R. Uhl, D. Jaeger, L. Luo, C. Gretener, S. Buecheler, Y.E. Romanyuk, A.N. Tiwari, Highly transparent and conductive ZnO: Al thin films from a low temperature aqueous solution approach, *Adv. Mater.* 26 (2014) 632–636, <https://doi.org/10.1002/adma.201303186>.
- [24] Z. Yang, S. Gao, T. Li, F.Q. Liu, Y. Ren, T. Xu, Enhanced electron extraction from template-free 3D nanoparticulate transparent conducting oxide (TCO) electrodes for dye-sensitized solar cells, *ACS Appl. Mater. Interfaces* 4 (2012) 4419–4427, <https://doi.org/10.1021/am301090a>.
- [25] J. Puetz, N. Al-Dahoudi, M.A. Aegerter, Processing of transparent conducting coatings made with redispersible crystalline nanoparticles, *Adv. Eng. Mater.* 6 (2004) 733–737, <https://doi.org/10.1002/adem.200400078>.
- [26] S. Ghanizadeh, T.A.N. Peiris, D.S.Y. Jayathilake, D.A. Hutt, K.G.U. Wijayantha, D.J. Southee, P.P. Conway, P. Marchand, J.A. Darr, I.P. Parkin, C.J. Carmalt, Dispersion and microwave processing of nano-sized ITO powder for the fabrication of transparent conductive oxides, *Ceram. Int.* 42 (2016) 18296–18302, <https://doi.org/10.1016/j.ceramint.2016.08.157>.
- [27] S. Du, Y. Tian, H. Liu, J. Liu, Y. Chen, Calcination effects on the properties of gallium-doped zinc oxide powders, *J. Am. Ceram. Soc.* 89 (2006) 2440–2443, <https://doi.org/10.1111/j.1551-2916.2006.01093.x>.
- [28] T. Königer, T. Rechtenwald, I. Al-Naimi, T. Frick, M. Schmidt, H. Münster, CO<sub>2</sub>-laser treatment of indium tin oxide nanoparticle coatings on flexible polyethyleneterephthalate substrates, *J. Coatings Technol. Res.* 7 (2010) 261–269, <https://doi.org/10.1007/s11998-009-9181-5>.
- [29] T. Park, D. Kim, Excimer laser sintering of indium tin oxide nanoparticles for fabricating thin films of variable thickness on flexible substrates, *Thin Solid Films* 578 (2015) 76–82, <https://doi.org/10.1016/j.tsf.2015.02.015>.
- [30] M. Schuster, S. Groß, F. Roider, I. Maksimenko, P. Wellmann, Tuning electrical and optical properties of transparent conductive thin films using ITO and ZnO nanoparticles, Sol-Gel-ZnO and Ag nanowires, *Int. J. Nanoparticles Nanotechnol.* 3 (2017) 1–11, <https://doi.org/10.35840/2631-5084/5513>.
- [31] E.J. Kim, J.H. Kim, A.M. Azad, Y.S. Chang, Facile synthesis and characterization of Fe/FeS nanoparticles for environmental applications, *ACS Appl. Mater. Interfaces* 3 (2011) 1457–1462, <https://doi.org/10.1021/am200016v>.
- [32] T. Minami, T. Miyata, T. Yamamoto, Stability of transparent conducting oxide films for use at high temperatures, *J. Vac. Sci. Technol. A Vacuum, Surfaces, Film.* 17 (1999) 1822–1826, <https://doi.org/10.1116/1.581897>.
- [33] S. Capone, A. Forleo, L. Francioso, R. Rella, P. Siciliano, J. Spadavecchia, D.S. Presicce, A.M. Taurino, Solid state gas sensors: state of the art and future activities, *J. Optoelectron. Adv. Mater.* (2003) 1335–1348, <https://doi.org/10.1002/chin.200429283>.
- [34] R. Costi, A.E. Saunders, U. Banin, Colloidal hybrid nanostructures: a new type of functional materials, *Angew. Chemie - Int. Ed.* 49 (2010) 4878–4897, <https://doi.org/10.1002/anie.200906010>.

- [35] I. Bica, E.M. Anitas, Magnetodielectric effects in membranes based on magnetorheological bio-suspension, *Mater. & Des.* 155 (2018) 317–324, <https://doi.org/10.1016/j.matdes.2018.06.005>.
- [36] J. Tauc, Optical properties and electronic structure of amorphous Ge and Si, *Mater. Res. Bull.* 3 (1968) 37–46, [https://doi.org/10.1016/0025-5408\(68\)90023-8](https://doi.org/10.1016/0025-5408(68)90023-8).
- [37] S.W. Bian, I.A. Mudunkotuwa, T. Rupasinghe, V.H. Grassian, Aggregation and dissolution of 4 nm ZnO nanoparticles in aqueous environments: influence of pH, ionic strength, size, and adsorption of humic acid, *Langmuir* 27 (2011) 6059–6068, <https://doi.org/10.1021/la200570n>.
- [38] R.A. Reichle, K.G. McCurdy, L.G. Hepler, Zinc hydroxide: solubility product and hydroxy-complex stability constants from 12.5–75 °C, *Can. J. Chem.* 53 (1975) 3841–3845, <https://doi.org/10.1139/v75-556>.
- [39] E. Tombácz, pH-dependent surface charging of metal oxides, *Period. Polytech. Chem. Eng.* 53 (2009) 77–86, <https://doi.org/10.3311/pp.ch.2009-2.08>.
- [40] R. Hong, T. Pan, J. Qian, H. Li, Synthesis and surface modification of ZnO nanoparticles, *Chem. Eng. J.* 119 (2006) 71–81, <https://doi.org/10.1016/j.cej.2006.03.003>.
- [41] G. Trefalt, F.J.M. Ruiz-Cabello, M. Borkovec, Interaction forces, heteroaggregation, and deposition involving charged colloidal particles, *J. Phys. Chem. B* 118 (2014) 6346–6355, <https://doi.org/10.1021/jp503564p>.
- [42] V.A. Hackley, J.D. Clogston, Measuring the hydrodynamic size of nanoparticles in aqueous media using batch-mode dynamic light scattering, *Methods Mol. Biol.* 697 (2011) 35–52, [https://doi.org/10.1007/978-1-60327-198-1\\_4](https://doi.org/10.1007/978-1-60327-198-1_4).
- [43] E.J.H. Lee, C. Ribeiro, E. Longo, E.R. Leite, Oriented attachment: an effective mechanism in the formation of anisotropic nanocrystals, *J. Phys. Chem. B* 109 (2005) 20842–20846, <https://doi.org/10.1021/jp0532115>.
- [44] T. Ogi, D. Hidayat, F. Iskandar, A. Purwanto, K. Okuyama, Direct synthesis of highly crystalline transparent conducting oxide nanoparticles by low pressure spray pyrolysis, *Adv. Powder Technol.* 20 (2009) 203–209, <https://doi.org/10.1016/j.apt.2008.09.002>.
- [45] W.J. Zhang, D.E. Miser, Coalescence of oxide nanoparticles: in situ HRTEM observation, *J. Nanopart. Res.* 8 (2006) 1027–1032, <https://doi.org/10.1007/s11051-005-9056-3>.
- [46] V.N. Koparde, P.T. Cummings, Phase transformations during sintering of titania nanoparticles, *ACS Nano* 2 (2008) 1620–1624, <https://doi.org/10.1021/nn800092m>.
- [47] H. Palneedi, J.H. Park, D. Maurya, M. Peddigari, G.T. Hwang, V. Annapureddy, J.W. Kim, J.J. Choi, B.D. Hahn, S. Priya, K.J. Lee, J. Ryu, Laser irradiation of metal oxide films and nanostructures: applications and advances, *Adv. Mater.* 30 (2018) 1705148–1–1705148–38, <https://doi.org/10.1002/adma.201705148>.
- [48] N. Xia, R.A. Gerhardt, Fabrication and characterization of highly transparent and conductive indium tin oxide films made with different solution-based methods, *Mater. Res. Express* 3 (2016) <https://doi.org/10.1088/2053-1591/3/11/116408>.
- [49] J. Wang, G. Chen, F. Sun, Z. Zhou, Z.Q. Liu, C. Liu, Combined effects of surface oxidation and interfacial intermetallic compound growth on solderability degradation of electrodeposited tin thin films on copper substrate due to isothermal ageing, *Corros. Sci.* 139 (2018) 383–394, <https://doi.org/10.1016/j.corsci.2018.05.020>.
- [50] P. Hovington, D. Drouin, R. Gauvin, CASINO: a new Monte Carlo code in C language for electron beam interaction – part I: description of the program, *Scanning* 19 (1997) 1–14, <https://doi.org/10.1002/sca.4950190101>.
- [51] S.C. Baker-Finch, K.R. McIntosh, D. Yan, K.C. Fong, T.C. Kho, Near-infrared free carrier absorption in heavily doped silicon, *J. Appl. Phys.* 116 (2014) <https://doi.org/10.1063/1.4893176> 063106-1-063106-12.
- [52] P.D. Nellist, S.J. Pennycook, The principles and interpretation of annular dark-field Z-contrast imaging, *Adv. Imaging Electron Phys.* 113 (2000) 147–203, [https://doi.org/10.1016/S1076-5670\(00\)80013-0](https://doi.org/10.1016/S1076-5670(00)80013-0).
- [53] H. Zhu, R.S. Averbach, Sintering processes of two nanoparticles: a study by molecular dynamics simulations, *Philos. Mag. Lett.* 73 (1996) 27–33, <https://doi.org/10.1080/095008396181073>.
- [54] A.P. Alivisatos, Naturally aligned nanocrystals, *Science* 289 (5480) (2000) 736–737, <https://doi.org/10.1126/science.289.5480.736>.
- [55] J.F. Banfield, S.A. Welch, H. Zhang, T.T. Ebert, R.L. Penn, Aggregation-based crystal growth and microstructure development in natural iron oxyhydroxide biomineralization products, *Science* 289 (5480) (2000) 751–754, <https://doi.org/10.1126/science.289.5480.751>.
- [56] J. Nolic, M. Mündlein, Electrically conductive adhesives, in: E. Suhir, Y.C. Lee, C.P. Wong (Eds.), *Micro- and Opto-electronic Materials and Structures: Physics, Mechanics, Design, Reliability, Packaging*, Springer, New York 2007, pp. 571–610.
- [57] L. Li, J.E. Morris, Electrical conduction models for isotropically conductive adhesive joints, *IEEE Trans. Compon. Packag. Manuf. Technol.: Part A* 20 (1997) 3–8, <https://doi.org/10.1109/95.558537>.
- [58] J.L. Becklehimer, R.B. Pandey, Percolation of chains and jamming coverage in two dimensions by computer simulation, *J. Stat. Phys.* 75 (1994) 765–771, <https://doi.org/10.1007/BF02186881>.
- [59] S.H. Park, J. Hwang, G.S. Park, J.H. Ha, M. Zhang, D. Kim, D.J. Yun, S. Lee, S.H. Lee, Modeling the electrical resistivity of polymer composites with segregated structures, *Nat. Commun.* 10 (2019) 2537–1–2537-11, <https://doi.org/10.1038/s41467-019-10514-4>.
- [60] D.S. McLachlan, M. Blaszkiewicz, R.E. Newnham, Electrical resistivity of composites, *J. Am. Ceram. Soc.* 73 (1990) 2187–2203, <https://doi.org/10.1111/j.1151-2916.1990.tb07576.x>.